Volume 41
Number 2
February 2026
Pages 537–806

JAAS

Journal of Analytical Atomic Spectrometry

rsc.li/jaas

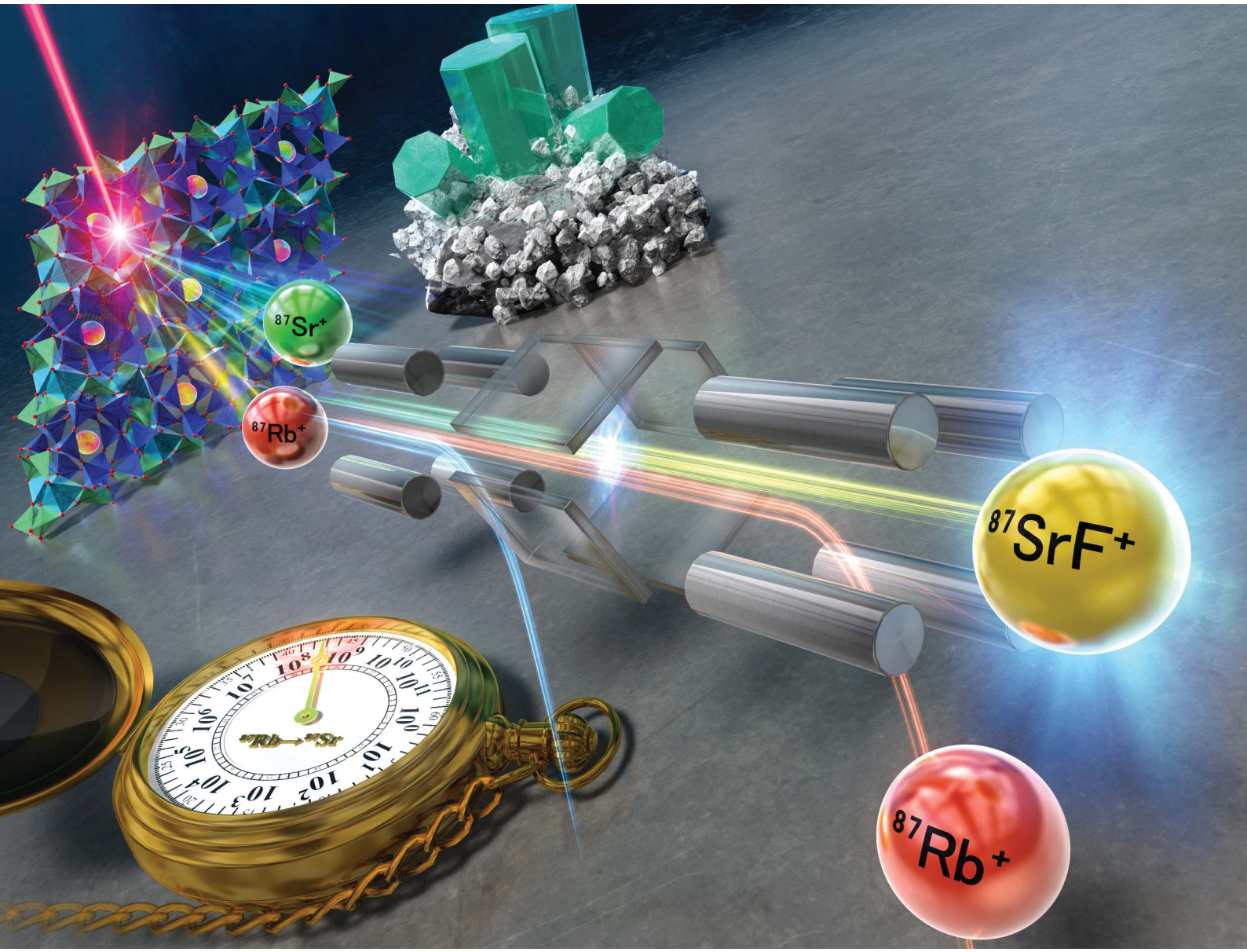

ISSN 0267-9477

ROYAL SOCIETY OF CHEMISTRY

PAPER

Yueheng Yang *et al.*

In situ Rb–Sr beryl geochronology by LA-ICP-MS/MS

JAAS

PAPER

View Article Online
View Journal | View Issue

Cite this: *J. Anal. At. Spectrom.*, 2026, **41**, 601

In situ Rb–Sr beryl geochronology by LA-ICP-MS/MS

Menpin Zhang,[ab] Yueheng Yang,[*ab] Chao Huang,[ab] Shitou Wu,[ab] Zhuyin Chu,[ab] Zifu Zhao,[ac] Hao Wang,[ab] Lei Xu,[ab] Jinhui Yang[ab] and Fuyuan Wu[ab]

Beryl is a principal beryllium (Be) host in diverse geological settings, including pegmatite, mica schist, and tungsten (W)–tin (Sn) systems (typically as high-temperature hydrothermal veins), and may occur at metasomatic contacts between igneous intrusions and gneiss, schist, or carbonate rock. Despite extensive work on mineralogy and trace element systematics, the geochronological potential of beryl remains underexplored. Here, we establish and validate an *in situ* Rb–Sr dating protocol for beryl using LA-ICP-MS/MS. Eight natural beryl samples spanning 1.8–0.14 Ga with Rb contents of 30–500 ppm were analyzed. Samples YYX241, M6548, M7971, and WLST181 exhibit relatively low common-Sr contents from 0.64% to 11.4%, whereas HJLG241, CHY241, MFS251, and SHY241 display elevated and variable common Sr contents from 12.0% to 29.4%. Isochron-based evaluations show that *in situ* beryl Rb–Sr ages are precise and accurate and consistent with solution Rb–Sr results or U–Pb ages of coexisting accessory minerals, while providing high spatial resolution and analytical throughput with high efficiency and resolution. We additionally assess the Rb–Sr closure temperature in beryl. To facilitate routine application, we present a data reduction scheme (DRS) named "Visual Rb–Sr age" and a visual (inverse) isochron Rb–Sr simultaneous age with an initial Sr plug-in for Iolite to process *in situ* datasets. On the basis of isotope-dilution mass spectrometry (ID–MS) isochrons, beryl samples HJLG241 and CHY241, yielding Rb–Sr ages of 1793 ± 13 Ma (2s, $n = 5$) and 1835 ± 8 Ma (2s, $n = 5$), respectively, are proposed as candidate reference materials for microbeam Rb–Sr geochronology. These results demonstrate that direct Rb–Sr dating of beryl and its gem varieties (aquamarine, emerald, heliodor, goshenite, morganite, and red beryl) can provide independent age constraints that strengthen provenance and timing assessments in beryl-focused geochemical studies.

Received 31st August 2025
Accepted 12th November 2025

DOI: 10.1039/d5ja00334b

rsc.li/jaas

1. Introduction

Beryl [$Be_3Al_2Si_6O_{18}$], an important Be-bearing mineral, occurs widely in granitic pegmatites and mica schists.[1] It is also commonly associated with Sn and W ore bodies hosted by high-temperature hydrothermal veins and, less frequently, with metasomatic contacts between igneous intrusions and gneiss, schist, or carbonate rocks.[2] In granitic pegmatites, beryl typically coexists with quartz, potassium feldspar, albite, muscovite, biotite, and tourmaline. Beyond its geological significance, beryl is of economic importance: common (industrial) beryl is mined from pegmatites in Russia, Colombia, Brazil, and the United States, and elsewhere, while its gem varieties—including aquamarine, emerald, heliodor, goshenite, morganite, and red beryl—command substantial commercial value. Despite this prominence, research has largely emphasized beryl's mineralogy,[3] trace elements[4] and oxygen isotopic composition,[5] whereas its geochronological potential remains comparatively underexplored.

Recent advances in laser ablation inductively coupled plasma tandem mass spectrometry (LA-ICP-MS/MS) have enabled robust *in situ* Rb–Sr geochronology for K-rich or Rb-bearing rock-forming minerals (*e.g.*, micas) and increasingly for additional phases as well.[6–20] LA-ICP-MS/MS has gained traction due to its comparatively low cost, analytical efficiency, and broad accessibility.[21–23]

As first emphasized by Zack and Link (2019),[24] the alkali-rich nature of beryl renders it an attractive target for Rb–Sr dating: a survey of >50 global samples showed that ~90% contain between 5 and 50 ppm Rb coupled with extremely low Sr, yielding very high $^{87}Rb/^{86}Sr$ ratios (often>10 000). Under such conditions, single-sample (model) ages become feasible, wherein measured $^{87}Sr/^{86}Sr$ together with $^{87}Sr/^{87}Rb$ can be converted directly to ages assuming negligible initial (common) Sr. More recently, Daneshvar *et al.* (2021) (ref. 25) applied ID-TIMS Rb–Sr isochron methods to seven beryl samples from lithium–cesium–tantalum (LCT) pegmatite in the Ebrahim-Attar Mountain, western Iran. Unfortunately, six showed only

[a]*State Key Laboratory of Lithospheric and Environmental Coevolution, Institute of Geology and Geophysics, Chinese Academy of Sciences, Beijing, 100029, China. E-mail: yangyueheng@mail.iggcas.ac.cn*

[b]*College of Earth and Planetary Science, University of Chinese Academy of Sciences, Beijing, 100049, China*

[c]*School of Earth and Space Science, University of Science and Technology of China, Hefei, 230026, China*

weak positive arrays and did not yield a robust Rb–Sr isochron age.

Taken together, these studies highlight both the promise and the current paucity of systematic Rb–Sr geochronology for beryl. Here, integrating LA-ICP-MS/MS with isotope-dilution approaches, we present new Rb–Sr geochronological data for beryl and address the following objectives: (1) quantify Rb and common-Sr contents across diverse beryl samples; (2) assess the precision, accuracy, and limitations of *in situ* Rb–Sr ages relative to solution Rb–Sr and accessory-phase U–Pb constraints; (3) introduce a data reduction scheme (DRS) and a visual Rb–Sr age plugin for Iolite tailored to *in situ* datasets; (4) evaluate the Rb–Sr closure temperature in beryl; and (5) examine the feasibility of establishing primary Rb–Sr beryl reference materials for microanalytical Rb–Sr geochronology.

2. Experimental

Fragments from eight beryl chips were prepared for analysis. Crystal fragments were mounted in epoxy resin and polished to expose fresh interiors. Each mount was examined using transmitted- and reflected-light photomicrographs taken for each beryl sample. Rb–Sr ages were determined by ID-MS for two samples and by LA-ICP-MS/MS for all eight samples at the State Key Laboratory of Lithospheric and Environmental Coevolution (SKLLEC), Institute of Geology and Geophysics, Chinese Academy of Sciences (IGG–CAS), Beijing.

2.1 Sample descriptions

Table 1 summarizes the beryl specimens investigated in this study. Jining and the Wula Mountain in Inner Mongolia are key areas for early Cambrian geological research in North China. Paleoproterozoic-Mesoproterozoic granitic magmatic activity formed extensive bodies of potassium-rich granites and potassium-rich pegmatite veins. The five samples (HJLG241, CHY241, YYX241, M6548 and M7971) originate from this significant component of the North China Craton. The other three samples (MFS251, SHY241, and WST181) were obtained from China's renowned granitic pegmatite-type rare metal deposits.

The suite comprises two museum specimens from the IGG-CAS collection (M6548 and M7971) and six samples from our field collection (HJLG241, CHY241, YXX241, MFS251, SHY241, and WST181). All samples consist of relatively coarse grains, commonly up to 10–100 millimeters in size (Fig. 1). Inclusion-free chips were hand-picked under a binocular microscope, embedded in 1-inch epoxy mounts, sectioned to expose interiors, polished, and photographed. Prior to laser ablation, the mounts were rinsed in 2% HNO_3 for several minutes and thoroughly cleaned with ultrapure water.

Most crystals exhibit pale green to blue coloration (Fig. 1). Neither optical inspection nor BSE imaging revealed systematic compositional zoning. Preliminary trace-element analyses by LA-ICP-MS indicated Rb concentrations and older apparent ages in two samples (HJLG241 and CHY241); these were therefore selected for complementary Rb–Sr ID-TIMS analysis.

2.2 Major and trace element analysis

Major element determination and BSE imaging were performed on a Cameca SX Five electron microprobe (Fig. 1). Operating conditions include parameters of a 3×10^{-8} A beam current, a 15 kV acceleration voltage, and a 5 μm beam diameter. Calibration employed albite (Na) and hornblende (Si, Al, and Fe) standards from the National Bureau of Standards (USA), together with additional mineral or synthetic crystal standards. Data were corrected using the ZAF method.

Trace element concentrations were measured by coupling a 193 nm ArF excimer laser to an Element XR sector field (SF) ICP–MS. For both reference materials and unknowns, a 32 μm spot, a 5 Hz repetition rate, and a fluence of 4 J cm^{-2} were used. Each analysis comprised approximately 30 s of background acquisition followed by around 40 s of ablation signal (full parameters in SI Table S1). The ARM-1 reference material was analyzed after every ten unknowns. External calibration was performed against ARM-1 glass using the recommended values of Wu *et al.*,[26] with internal standardization to ^{29}Si based on SiO_2 contents determined by EPMA. Analytical accuracy and precision were monitored with the NIST SRM 610 reference glass, yielding combined uncertainties better than 10%. Trace element data reduction was carried out in Iolite software following Wu *et al.*[26]

2.3 Solution Rb–Sr measurement

All wet-chemical procedures were carried out in class-100 laminar-flow hoods maintained in a positive-pressure class-

Table 1 Lists the beryl samples investigated in this study[a]

Sample	Description and location	Host rock	Refer. age (Ma)	Methods
HJLG241	Heijialagou, Inner Mongolia, China	Pegmatite	~1800	Sol. and laser
CHY241	Chahanying, Inner Mongolia, China	Pegmatite	~1830	Sol. and laser
YYX241	Yiyuanxin, Inner Mongolia, China	Pegmatite	~1830	Laser
M6548	Xiaomiaozi, Inner Mongolia, China	Pegmatite	~1780	Laser
M7971	Jining, Inner Mongolia, China	Pegmatite	~240	Laser
MFS251	Mufushan, Hunan Province, China	Pegmatite	~150	Laser
SHY241	Shihuiyao, Inner Mongolia, China	Pegmatite	~150	Laser
WLST181	Weilasituo, Inner Mongolia, China	Pegmatite	~140	Laser

[a] M is the prefix of the IGG-CAS museum; the others are from our sampling.

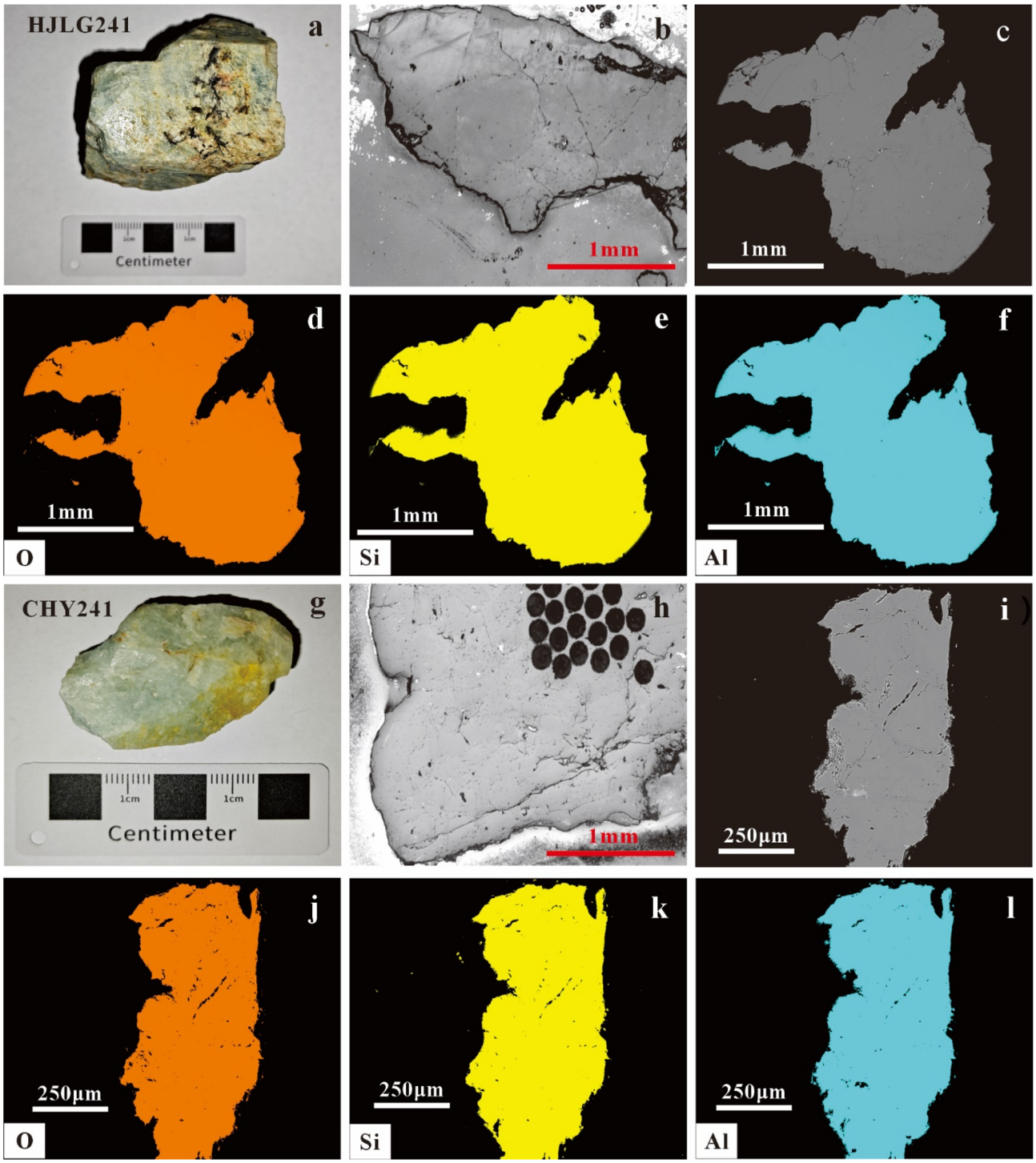

Fig. 1 Photographs and BSE images of the HJLG241 and CHY241 beryl samples.

1000 cleanroom. A concise overview of digestion, chromatographic separation, and mass spectrometric protocols is provided below; comprehensive descriptions are given in Yang *et al.*[27,28] and Chu *et al.*[29]

Approximately 100 mg of powdered beryl chips or NBS607 were weighed (±0.1 mg) into 5 mL Savillex PFA vials together with appropriate amounts of a mixed ^{84}Sr–^{87}Rb spike. Samples were dissolved in 0.4 mL of 22 M HF plus 0.2 mL of 14 M HNO_3 at 150 °C on a hotplate for one week. After cooling, solutions were evaporated to dryness at 120 °C, re-dissolved in 1 mL of 14 M HNO_3, and dried again; this step was repeated once. The residues were finally taken up in 1 mL of 3 M HNO_3 for ion-exchange separation.

Ion chromatography was performed using Bio-Rad polypropylene columns freshly packed with 1 mL of Sr-specific resin. The columns were pre-washed with 2 mL 3 M HNO_3,

rinsed three times with 2 mL ultrapure H_2O, and conditioned with 2 mL 3 M HNO_3. Samples dissolved in 0.5 mL 3 M HNO_3 were loaded, followed by two 0.1 mL 3 M HNO_3 washes. Rb was eluted with 2 mL 3 M HNO_3. Barium (Ba) and any residual Rb were removed with 5 mL 7 M HNO_3; Sr was subsequently collected with 2.5 mL ultrapure H_2O.

Rb cuts were dried, re-dissolved, and diluted to ~200 ppb in 2% HNO_3 for MC-ICP-MS. Sr cuts underwent a second pass through the Sr-resin protocol to ensure complete Rb removal and then were evaporated to dryness for TIMS. The $^{87}Rb/^{85}Rb$ ratios were measured on a Neptune Plus MC-ICP-MS. A 200 ppb NBS984 Rb solution was run routinely to optimize sensitivity and stability.[30] Rb concentrations were calculated *via* isotope dilution equations from spike-corrected $^{87}Rb/^{86}Sr$. Rb concentrations were calculated directly *via* isotope dilution equations using the measured signals and the mixed spike. The $^{87}Rb/^{86}Sr$ ratios were then derived from these calculated concentrations of ^{87}Rb and ^{86}Sr. Sr isotopes were measured on a Triton Plus TIMS. Sr was loaded on tungsten (W) single filaments from 2 μL of 2.5 M HCl with TaF_5 as an emitter. During Sr acquisition, potential Rb^+ interference on $^{87}Sr^+$ was monitored by measuring m/z 85 (^{85}Rb); Rb was evaporated to maintain $^{85}Rb/^{86}Sr < 5 \times 10^{-4}$, limiting the $^{87}Rb^+$ contribution to < 20 ppm and rendering interference correction negligible.[29]

Isotope fractionation was corrected using the exponential law, normalizing to $^{86}Sr/^{88}Sr = 0.1194$ after subtracting the spike contribution from the natural Sr.[29,31] The measured $^{87}Sr/^{86}Sr$ of SRM987 during the analytical sessions was 0.710250 ± 0.000012 (2s, $n = 8$), in excellent agreement with published values.[27–29] Rb–Sr isotopic data for NBS607 potassium feldspar yielded Rb = 528.5 ppm, Sr = 66.13 ppm, and $^{87}Sr/^{86}Sr = 1.2012$ ± 0.00003 (2s).[29] Procedural Sr blanks were <100 pg.

2.4 *In situ* Rb–Sr measurement

In situ Rb–Sr dating of beryl was carried out using either a 193 nm ArF excimer laser (Analyst G2, Photon Machines) or a 257 nm NWR Femto femtosecond laser (Elemental Scientific Lasers) equipped with a TwoVol2 sample chamber, coupled to a triple-quadrupole ICP-MS/MS (iCAP TQ, Thermo Scientific).[17,18] Full instrumental parameters are provided in SI Table S1; a brief summary follows.

ICP-MS/MS conditions were first optimized in single-quadrupole, no-gas mode to establish robust plasma operation (U/Th ≈ 1 on NIST 610) and low oxide formation (ThO^+/Th^+ < 0.5%). During routine analysis, Q1 of the iCAP TQ was operated in "normal" resolution (~10 amu transmission window) and Q2 at 0.7 amu. The instrument was then switched to TQ mode with SF_6 as the reaction gas for collision-reaction cell tuning (*e.g.*, entry lens), maximizing the yield of Sr reaction products while maintaining negligible Rb reactivity at a mass shift of +19.[7,17] High-purity SF_6 (99.995%) was used as the reaction gas, and a small N_2 flow (4.0 mL min^{-1}) was added to the carrier gas downstream of the sample chamber to enhance sensitivity.[32]

The reaction product $^{87}SrF^+$ (*e.g.*, mass-shifted (87 + 19) to $m/z \approx 106$) was monitored to separate ^{87}Sr from isobaric ^{87}Rb. To mitigate potential memory effects from Rb-based SF_6 reaction products that could overlap the SrF^+ signal, a short dwell time of 1 ms was used for ^{87}Rb. Laser parameters were adjusted to sample composition: spot diameters of 110–150 μm, repetition rates of 10 Hz, and a fluence of ~4 J cm^{-2} were typical. The ^{85}Rb signal was measured as a proxy for ^{87}Rb, and the present-day natural ratio $^{87}Rb/^{85}Rb = 0.3861$ was applied to calculate ^{87}Rb from measured ^{85}Rb. The system operated in a fully automated, trigger-synchronized mode between the G2 nanosecond or NWR femtosecond laser and the iCAP TQ to facilitate high-throughput analyses.[17,18]

Each analysis comprised 15 s of background acquisition, 75 s of on-peak ablation, and 30 s of aerosol washout. A bracketing strategy was employed whereby, after every five unknown analyses, one to two reference material analyses (NIST 610, HJLG241, or CHY241) were inserted, with additional reference runs at the beginning and end of each sequence. NIST 610 served as the primary reference material to correct instrumental drift; HJLG241 beryl was used to calibrate for matrix-dependent fractionation behavior; and CHY241 was treated as an unknown reference to monitor session-long data quality.

2.5 Data reduction with a DRS and visual Rb–Sr age plugin

Rb–Sr isotopic data were processed using Iolite version 4.11 using the "*in situ* Rb–Sr dating 2" data reduction scheme (DRS).[33] Iolite was used to calculate gas-blank-corrected intensities and raw isotopic ratios (*e.g.*, $^{87}Rb/^{87}Sr$) together with their associated uncertainties. Subsequent corrections, including elemental fractionation, matrix bias between NIST 610 and beryl, estimation of common Sr contents (%) ($f^{87}Sr_{sample} = (^{86}Sr/^{87}Sr)_{sample}/1.41844 \times 100$, assumption of the $(^{87}Sr/^{86}Sr)_{comm.} = 0.705$ or $(^{86}Sr/^{87}Sr)_{comm.} = 1.41844$), and mitigation of potential interference of $^{(87+19)}RbF^+$ on $^{(87+19)}Sr\,F^+$, were implemented within the Visual Rb–Sr age DRS.

Beryl Rb–Sr ages, which may be affected by variable common Sr, were calculated in IsoplotR using inverse-isochron regression.[34,35] This approach minimizes the strong error correlation between $^{87}Rb/^{86}Sr$ and $^{87}Sr/^{86}Sr$ that can mask geological dispersion on conventional isochron plots.

To facilitate objective signal-interval selection and avoid inclusion-related artifacts, a dedicated Iolite plugin ("Visual Rb–Sr age") was developed, analogous to the VizualAge plugin for U–Th–Pb dating. The Visual Rb–Sr age interface (Fig. 2) allows plotting on isochron or inverse-isochron diagrams (using Vermeesch's regression algorithm), with manual selection of *x*- and *y*-axes and optional anchoring for inverse-isochron. The estimated Rb–Sr ages are updated automatically as signal intervals are interactively selected (Fig. 2). In combination, the Visual Rb–Sr age plugin and the "Visual Rb–Sr age" DRS enable an end-to-end Iolite workflow, obviating the need for secondary processing (*e.g.*, in Excel). The plug-in code is available on request from Shitou Wu (shitou.wu@mail.iggcas.ac.cn) or ChemLab (liangy@chemlabcorp.com).[36]

The calculation of $^{87}Rb/^{87}Sr$ and $^{86}Sr/^{87}Sr$ ratios is shown in eqn (1)–(6). Due to the low natural abundance of ^{87}Rb (27.83%), its intensity is derived from ^{85}Rb (72.17%) measurements using

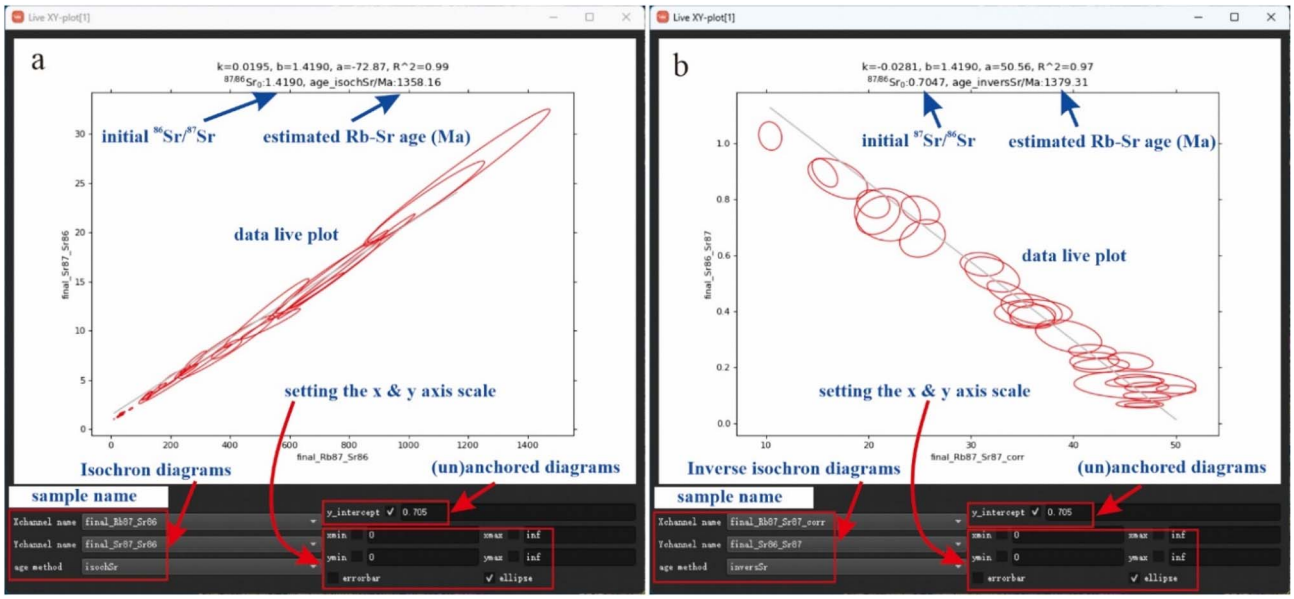

Fig. 2 Main features of the visual Rb–Sr age plugin for Iolite.

an $^{85}Rb/^{87}Rb$ ratio of 2.59 (eqn (1)). Both ^{86}Sr and ^{87}Sr are quantified *via* their $^{86}Sr^{19}F$ and $^{87}Sr^{19}F$ reaction products (eqn (4)). The raw $^{87}Rb/^{87}Sr$ ratio is first calculated using eqn (1), followed by determination of the element fractionation factor from the matrix-matched reference material HJLG241 (eqn (2)). The corrected $^{86}Sr/^{87}Sr$ ratio is obtained by multiplying the raw ratio with the fractionation factor (F_1), as outlined in (eqn (3)).

$$^{87}Rb/^{87}Sr_{\_r} = (^{85}Rb/2.59)/(^{87}Sr^{19}F) \quad (1)$$

$$F_1 = (^{87}Rb/^{87}Sr_{\_r,HJLG241})/(^{87}Rb/^{87}Sr_{\_t,HJLG241}) \quad (2)$$

$$^{87}Rb/^{87}Sr_{\_c,sample} = {}^{87}Rb/^{87}Sr_{\_r,sample}/F_1 \quad (3)$$

Here, F_1 = fractionation factor, which is calibrated using the reference material HJLG241.

The raw $^{86}Sr/^{87}Sr$ ratio is calculated using eqn (4). The fractionation factor is derived from the glass reference material NIST SRM 610 (eqn (5)). The corrected $^{86}Sr/^{87}Sr$ ratio is obtained by applying the fractionation factor (F_2) to the raw ratio, as delineated in eqn (6).

$$^{86}Sr/^{87}Sr_{\_r} = (^{86}Sr^{19}F)/(^{87}Sr^{19}F) \quad (4)$$

$$F_2 = (^{86}Sr/^{87}Sr_{\_r,610})/(^{86}Sr/^{87}Sr_{\_t,610}) \quad (5)$$

$$^{86}Sr/^{87}Sr_{\_c,sample} = {}^{86}Sr/^{87}Sr_{\_r,sample}/F_2 \quad (6)$$

Here, F_2 = fractionation factor, which is calibrated using reference materials NIST SRM 610.

All data were processed using Iolite 4.11 (ref. 33) with the in-house DRS "Visual Rb–Sr age" (DRS denotes "Data Reduction Schemes," a term specific to Iolite v4.11 data processing software). Ages were computed and plotted using the IsoplotR package.[34] Uncertainties were combined in quadrature following Horstwood *et al.*[37] and Rösel and Zack.[13] Long-term excess variances for the reference material NIST SRM 610 were derived from all measurement sessions, yielding values of 0% for the $^{86}Sr/^{87}Sr$ ratio. Additional systematic uncertainties include those associated with decay constants of the ^{87}Rb–^{87}Sr system (~0.4%). The data reduction strategy and uncertainty propagation workflow are detailed in Fig. 3.

Instrumental drift in elemental and isotopic ratios was corrected against NIST 610. Mass bias in $^{87}Rb/^{86}Sr$ and isotopic fractionation in $^{87}Sr/^{86}Sr$ were externally corrected using the recommended values for NIST 610 of 0.233 ± 0.001 (2s) and 0.70970 ± 0.000020 (2s), respectively.[38,39] To correct for matrix-dependent mass bias in $^{87}Rb/^{87}Sr$ between NIST 610 and beryl, the matrix-matched beryl reference material HJLG241 was used to determine the common Sr-corrected $^{87}Rb/^{87}Sr$ ratio. The element fractionation factor was calculated from the offset between the measured and true $^{87}Rb/^{87}Sr$ ratio (the latter estimated from the recommended age). For samples exhibiting variable common Sr, anchored inverse-isochron plots were produced in IsoplotR.[34,35]

3. Results and discussion

3.1 Chemical compositions

Major oxide and trace element data for the analysed beryl grains are presented in Table 2. The specimens are characterized by high SiO_2 (61.11 to 67.23 wt%) and Al_2O_3 (16.81 to 18.23 wt%). Beryllium concentrations vary between 50 165 and 55 710 ppm. The Na_2O (0.130–1.475 wt%) and K_2O (0.002–0.051 wt%) contents are uniformly low. Magnesium contents range from 18.6 to 660 ppm, MnO from 0.001 to 0.015 wt%, and FeO from 0.01 to 1.11 wt%. Li and Cs concentrations are highly variable, spanning 39.6 to 4843 ppm and 94.8 to 22 400 ppm, respectively. Rubidium concentrations range from 17.8 to 531 ppm,

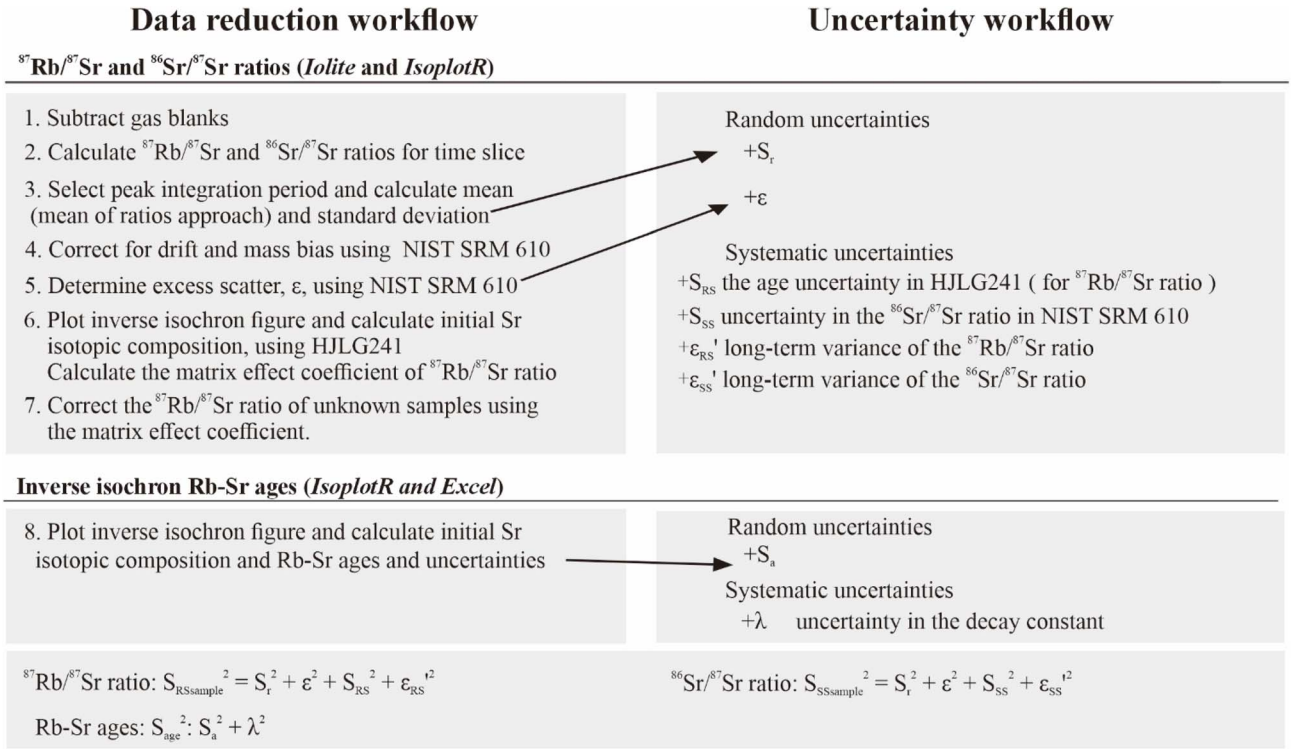

Fig. 3 The data reduction strategy and uncertainty propagation workflow.

Table 2 Major (%) and trace element (ppm) analysis compositions of beryl samples in this study[a]

	HJLG241	CHY241	YYX241	M6548	M7971	MFS251	SHY241	WLST181
EPMA								
SiO_2 (%)	65.99	67.23	65.29	64.37	61.11	66.13	66.21	66.31
Al_2O_3 (%)	18.02	17.74	16.83	16.81	17.14	17.69	18.18	18.23
Na_2O (%)	0.14	0.12	0.23	0.25	1.36	0.99	0.19	0.19
FeO (%)	0.58	0.76	1.11	0.88	0.01	0.76	0.28	0.17
Total	84.76	85.89	83.52	82.43	79.71	85.55	84.87	84.86
LA-ICP-MS								
Li (ppm)	59.6	39.6	102	67.1	4843	1985	273	161
Be (ppm)	55 470	54 600	55 710	57 742	48 790	50 165	54 451	54 211
Na_2O (%)	0.186	0.130	0.253	0.210	1.475	0.992	0.194	0.142
Mg (ppm)	432	146	26.0	660	115	162	18.6	381
Al_2O_3 (%)	18.9	17.8	18.2	18.2	19.0	17.7	18.2	18.2
SiO_2 (%)	64.7	66.2	64.6	64.6	64.8	66.1	66.2	66.3
K_2O (%)	0.051	0.002	0.007	0.004	0.035	0.027	0.009	0.006
Sc (ppm)	1.09	0.55	5.53	6.20	0.91	1.4	409	66.4
V (ppm)	1.04	1.30	8.11	8.66	3.70	8.25	13.9	296
MnO (%)	0.006	0.005	0.015	0.005	0.008	0.008	0.007	0.001
FeO (%)	0.54	0.65	1.14	0.79	0.02	0.76	0.28	0.17
Co (ppm)	1.80	1.95	0.82	1.15	10.5	0.52	0.81	0.30
Cu (ppm)	0.85	1.10	0.53	0.46	6.88	1.29	0.02	0.01
Zn (ppm)	2823	150	111	64.5	381	668	67.8	149
Rb (ppm)	48.7	17.8	31.6	42.6	531	132	63.4	47.3
Sr (ppm)	1.11	2.01	0.44	0.49	0.89	0.19	0.38	0.12
Zr (ppm)	1.74	0.26	0.87	0.68	3.11	0.19	0.21	0.08
Nb (ppm)	2.11	0.21	0.16	0.40	0.50	0.74	0.10	0.05
Cs (ppm)	94.8	97.0	650	118	22 400	2224	1290	1052

[a] Only measurement by LA-SF-ICP-MS; other measurements by both EPMA and LA-SF-ICP-MS.

with the sample M7971 containing several hundred ppm of Rb. The concentrations of V (1.04–296 ppm), Zn (64.5–2823 ppm), Sr (0.12–2.01 ppm), and Nb (0.05–2.11 ppm) are consistently low. Rare earth elements (REEs) are generally scarce and often occur below detection limits. The LA–ICP-MS results for the major elements SiO_2, Al_2O_3, Na_2O, and FeO are consistent with those determined by EMPA (Table 2).

The rubidium (Rb) content in rose-colored beryl (*e.g.*, morganite, colored by Mn^{2+}) is significantly higher than that in common beryl varieties (*e.g.*, emerald and aquamarine). This difference is primarily attributed to crystal-chemical substitution mechanisms and coloration processes. The structural channels in beryl can accommodate alkali metal ions (Na^+, K^+, Rb^+, and Cs^+). In rose-colored beryl, the substitution of Mn^{2+} for Al^{3+} creates charge imbalance, which requires charge compensation by Rb^+ and other large-radius alkali metal ions.[3,25] In contrast, the blue color of common beryl (*e.g.*, aquamarine) results from Fe^{2+}/Fe^{3+} chromophores, where charge balance is maintained through Fe^{3+} valence changes rather than alkali metal incorporation, leading to lower Rb contents.[1]

Furthermore, rose-colored beryl typically occurs in highly fractionated LCT-type pegmatites (enriched in Li, Cs, Rb, and Ta), which inherently have higher Rb background concentrations. Common beryl varieties (*e.g.*, emerald) often form in hydrothermal or non-LCT pegmatite environments with naturally lower Rb abundances. Therefore, the Rb content variation not only reflects differences in crystal-chemical mechanisms but also serves as an important indicator for discriminating beryl genesis and assessing the pegmatite evolution degree.

3.2 Solution Rb–Sr measurement

Five analyses of HJLG241 and CHY241 beryl chips were carried out by solution Rb–Sr analysis in this study. The Rb and Sr contents, as well as the $^{87}Rb/^{86}Sr$ and $^{87}Sr/^{86}Sr$ ratios, were corrected for blank contributions.[29] The ID-MS measurement results for the HJLG241 and CHY241 beryl samples are presented in Table 3.

Five measurements of HJLG241 yielded Rb and Sr contents of 26.82 ± 4.20 ppm (2s) and 2.740 ± 0.689 ppm (2s), respectively, together with isotopic ratios of $^{87}Rb/^{86}Sr = 31 \pm 13$ (2s)

Table 3 Rb–Sr data of the beryl samples obtained by ID-MS analyses

Sample	No.	Rb [ppm]	2s	Sr [ppm]	2s	$^{87}Rb/^{86}Sr$	2s	$^{87}Sr/^{86}Sr$	2s	Age (Ma)	±2s	$(^{87}Sr/^{86}Sr)_0$ (±2s)
	1	27.27	0.14	3.090	0.004	27.24	0.13	1.39220	0.00013	1783.2	8.4	
	2	23.85	0.13	2.965	0.005	24.71	0.12	1.33733	0.00014	1808.5	8.7	
HJLG241	3	29.37	0.16	2.526	0.004	36.71	0.19	1.63927	0.00020	1798.7	9.2	
	4	25.76	0.12	2.869	0.003	27.78	0.12	1.41539	0.00013	1807.2	7.7	
	5	27.83	0.15	2.250	0.003	39.25	0.20	1.69977	0.00079	1791.3	9.1	
Mean ± 2s		26.82	4.20	2.740	0.689	31	13	1.50	0.32	1797	21	0.707 (0.005)
	1	24.36	0.14	1.216	0.002	67.91	0.37	2.46374	0.00085	1830.0	9.9	
	2	24.22	0.14	1.212	0.002	67.79	0.37	2.47448	0.00197	1844.2	10.1	
CHY241	3	24.01	0.13	1.226	0.002	66.16	0.34	2.42327	0.00089	1835.1	9.4	
	4	24.32	0.12	1.224	0.001	67.31	0.32	2.45443	0.00092	1836.4	8.7	
	5	24.33	0.12	1.235	0.002	66.61	0.33	2.42869	0.00080	1828.5	9.01	
Mean ± 2s		24.25	0.29	1.223	0.018	67.15	1.51	2.449	0.044	1835	12	0.705 (0.006)

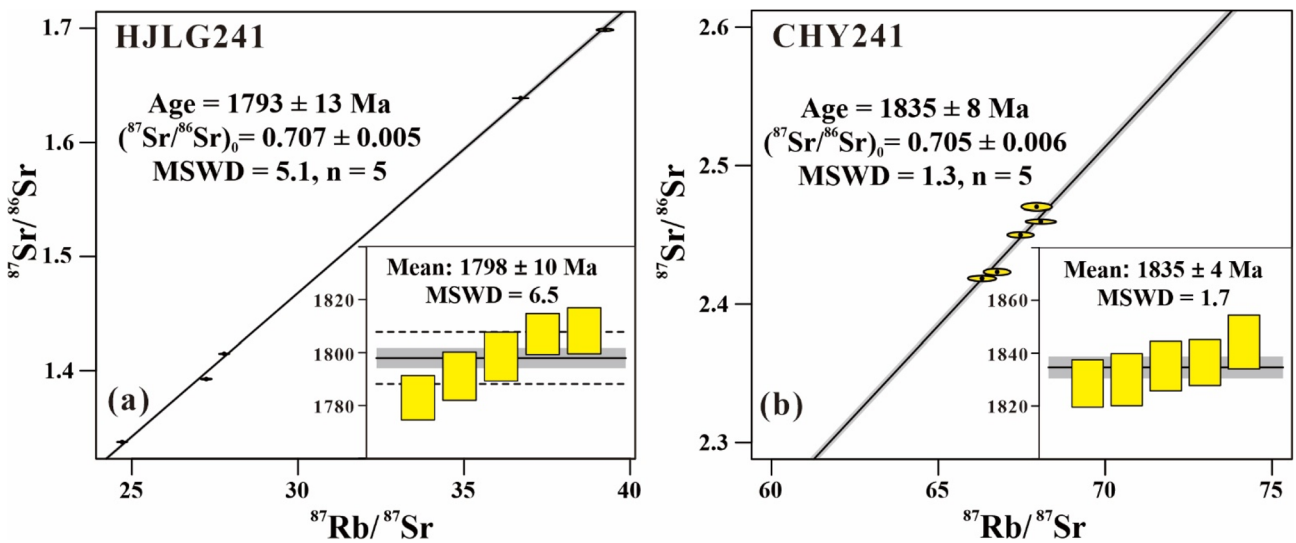

Fig. 4 Rb–Sr results of HJLG241 and CHY241 beryl samples obtained by isotope dilution methods. The errors represent 2s.

and $^{87}Sr/^{86}Sr = 1.50 \pm 0.32$ (2s). The initial $^{87}Sr/^{86}Sr$ ratio was calculated to be 0.707 ± 0.005 (2s). As illustrated in Fig. 4a, an anchored isochron diagram yielded an age of 1793 ± 13 Ma (2s, $n = 5$, MSWD = 5.1), consistent with the common-Sr-corrected weighted mean age of 1798 ± 10 Ma (2s, MSWD = 6.5) (for example $(^{87}Sr/^{86}Sr)_{corr.} = (^{87}Sr/^{86}Sr)_{sample} \times (1-f^{87}Sr)$). The result is also consistent with the 1752 ± 30 Ma U–Pb age of HJLG monazite as determined by LA–SF–ICP-MS (SI Table S2). Similarly, five analyses of CHY241 yielded Rb and Sr contents of 24.25 ± 0.29 ppm (2s) and 1.223 ± 0.018 ppm (2s), respectively, with isotopic ratios of $^{87}Rb/^{86}Sr = 67.15 \pm 1.51$ (2s) and $^{87}Sr/^{86}Sr = 2.449 \pm 0.044$ (2s). The initial $^{87}Sr/^{86}Sr$ ratio was 0.705 ± 0.006 (2s). As shown in Fig. 4b, an anchored isochron diagram produced an age of 1835 ± 8 Ma (2s, MSWD = 1.3), consistent with the common-Sr-corrected weighted mean age of 1835 ± 4 Ma (2s, MSWD = 1.7).

3.3 *In situ* Rb–Sr measurement

Anchored and unanchored inverse-isochron plots for the *in situ* Rb–Sr datasets are shown in Fig. 5 and 6, with the full analytical results reported in SI Table S3. Table 4 summarizes session-averaged Rb concentrations, the proportion of common Sr ($f^{87}Sr$), $^{87}Rb/^{87}Sr$ and $^{86}Sr/^{87}Sr$ ratios, and anchored/unanchored inverse-isochron ages for the eight beryl samples. The relationship between Rb content and $f^{87}Sr$ is illustrated in Fig. 7.

For the HJLG241 beryl, three analytical sessions produced unanchored inverse isochron ages of 1788 ± 35 Ma ($n = 20$; MSWD = 0.35), 1804 ± 31 Ma ($n = 17$; MSWD = 0.79), and 1799 ± 25 Ma ($n = 26$; MSWD = 0.47), with corresponding initial $^{87}Sr/^{86}Sr$ ratios of 0.750 ± 0.063, 0.699 ± 0.070, and 0.710 ± 0.051, respectively (Fig. 5a–c). Anchored inverse isochron diagrams yielded ages of 1803 ± 27 Ma ($n = 20$; MSWD = 0.41), 1801 ± 27 Ma ($n = 17$; MSWD = 0.69), and 1799 ± 21 Ma ($n = 26$; MSWD = 0.43). These are consistent with the ID–MS age of 1793 ± 13 Ma (2σ, $n = 5$) (Fig. 4a). The HJLG241 beryl displays variable common Sr, with $f^{87}Sr$ values from 2.1% to 40% with a median of $17.3 \pm 26.3\%$ (2σ, $n = 20$), from 0.76% to 68.9% with a median of $15.4 \pm 39.4\%$ (2σ, $n = 17$), and from 0.8% to 76.2% with a median of $14.9 \pm 35.0\%$ (2σ, $n = 26$), respectively (Table 4).

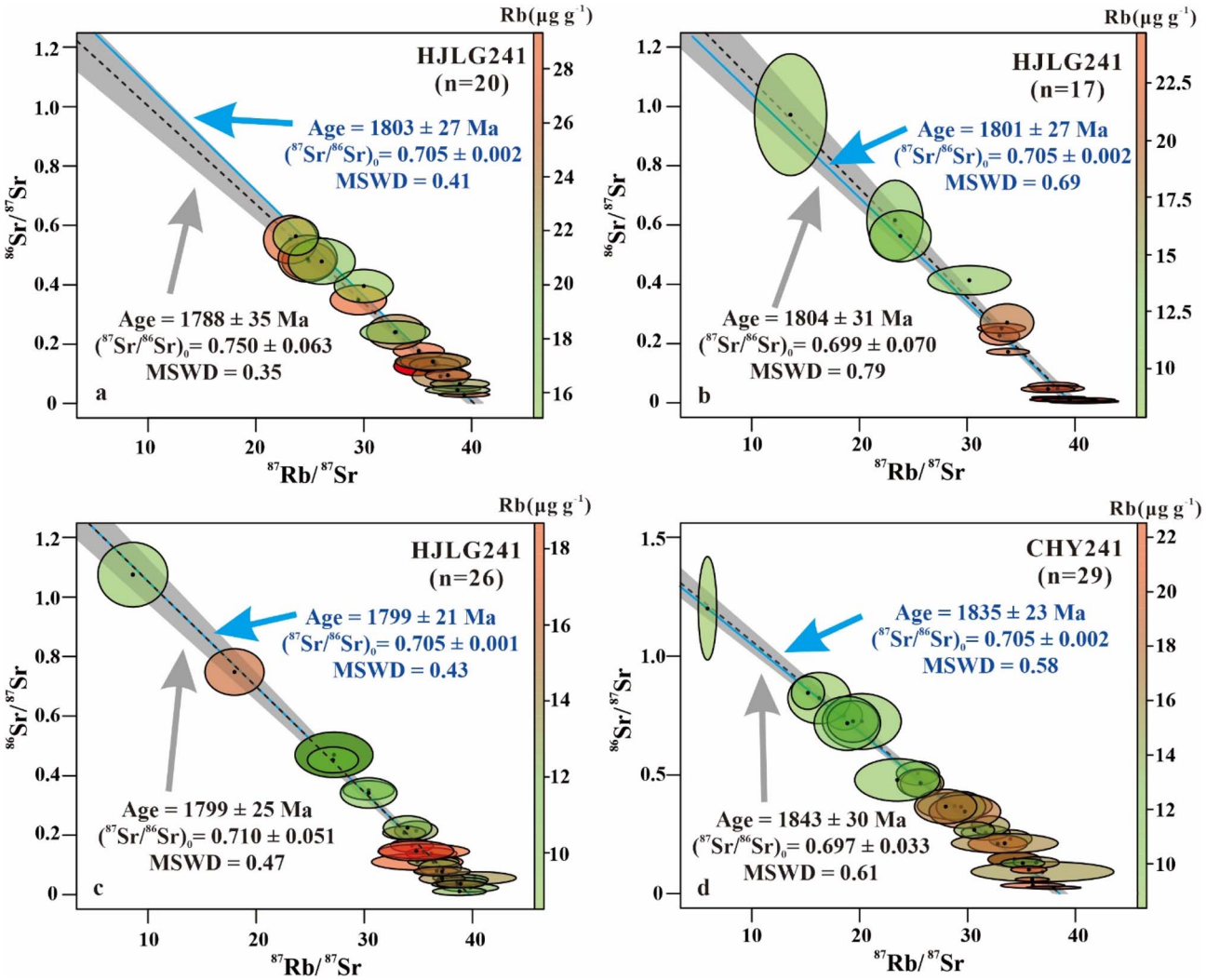

Fig. 5 Inverse isochron diagrams for HJLG241 (a–c) and CHY241 (d) beryl samples. Both unanchored and anchored inverse Rb–Sr calculations are shown for comparison. The errors represent 2s.

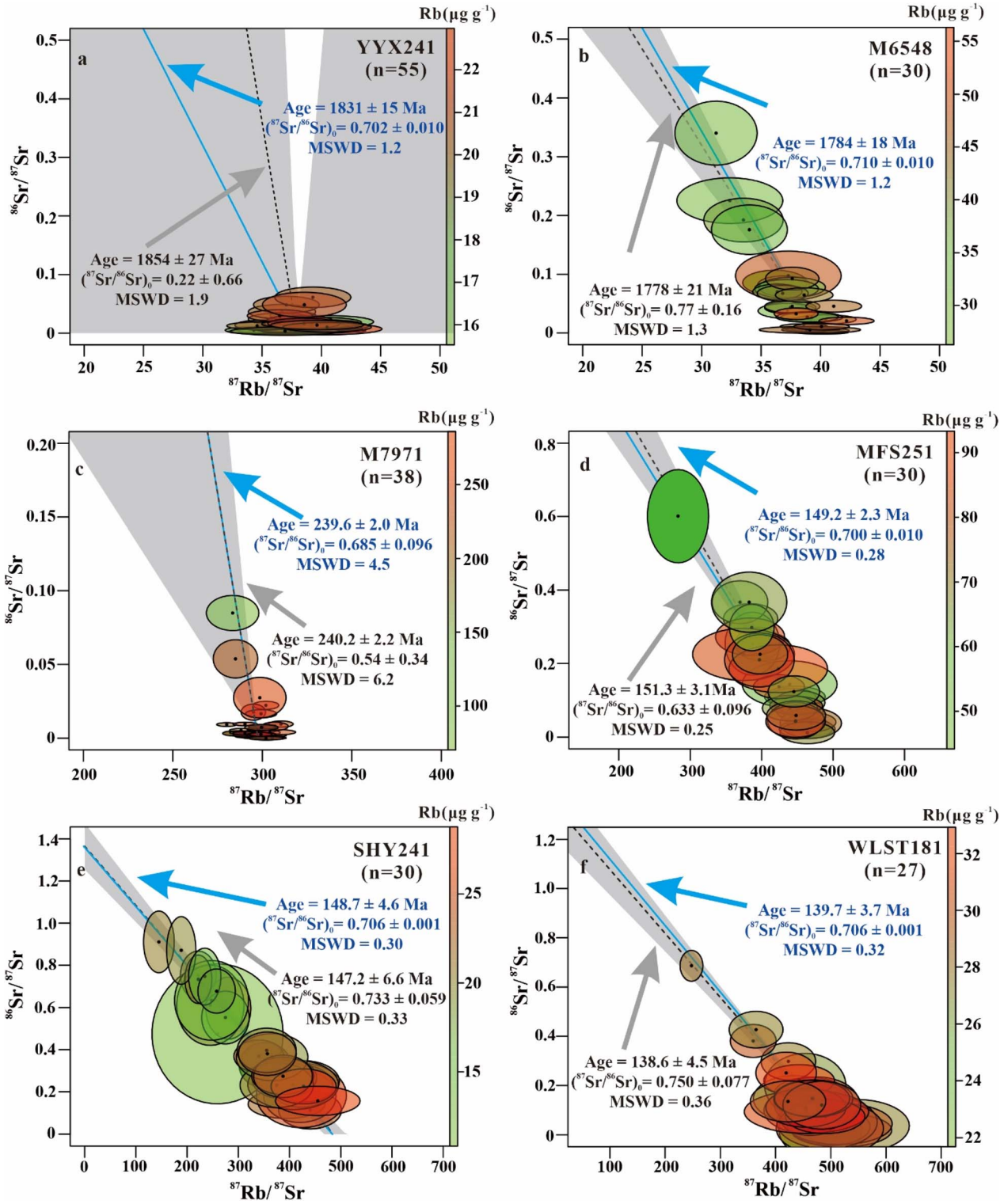

Fig. 6 Inverse isochron diagrams for YYX241 (a), M6548 (b), M7971 (c), MFS251 (d), SHY241 (e) and WLST181 (f) beryl samples. Both unanchored and anchored inverse Rb–Sr calculations are shown for comparison. The errors represent 2s.

The CHY241 beryl gave an unanchored inverse isochron age of 1843 ± 30 Ma (n = 29; MSWD = 0.7), with an initial $^{87}Sr/^{86}Sr$ ratio of 0.697 ± 0.033 (Fig. 5d). The anchored diagram yielded an age of 1835 ± 23 Ma (n = 29; MSWD = 0.6). Both are consistent with the ID–MS age of 1835 ± 8 Ma (2σ, n = 5) (Fig. 4b). The CHY241 beryl shows variable common Sr contents, ranging from 2.1% to 40%, with a median $f^{87}Sr$ value of 27.7 ± 41.7% (2σ, n = 63) (Table 4 and Fig. 7).

For the YYX241 beryl, the unanchored diagram gave an age of 1854 ± 27 Ma (n = 30; MSWD = 1.9), with an initial $^{87}Sr/^{86}Sr$

Table 4 Rb–Sr data of the beryl samples by LA-ICP-MS/MS

Samples	N	Laser[a]	$^{87}Rb/^{87}Sr$ (±2s)	$^{86}Sr/^{87}Sr$ (±2s)	Rb ppm (±2s)	$f^{87}Sr$ (%) (±2s)	Inverse age (±2s) Ma	Anchored inverse age (±2s) Ma
HJLG241	20	fs	32.3 (11.1)	0.244 (0.371)	23.6 (8.0)	17.3 (26.3)	1788 (35)	1803 (27)
HJLG241	17	fs	33.5 (14.9)	0.217 (0.556)	18.6 (10.2)	15.4 (39.4)	1804 (31)	1801 (27)
HJLG241	26	ns	33.4 (14.0)	0.210 (0.494)	13.6 (5.1)	14.9 (35.0)	1799 (25)	1799 (21)
CHY241	29	fs	27.9 (15.9)	0.391 (0.588)	15.0 (6.9)	27.9 (41.7)	1843 (30)	1835 (23)
YYX241	55	fs	38.1 (3.1)	0.0126 (0.0249)	19.5 (3.6)	0.89 (1.76)	1854 (19)	1830 (15)
M6548	30	fs	37.8 (5.0)	0.0666 (0.1530)	40.5 (13.0)	4.73 (10.85)	1778 (21)	1784 (18)
M7971	38	ns	297 (14)	0.0091 (0.0321)	224 (64)	0.64 (2.28)	240.2 (0.9)	238.9 (0.8)
MFS251	30	ns	421 (83)	0.169 (0.270)	70.0 (22.9)	12.0 (19.2)	151.3 (3.1)	149.2 (2.3)
SHY241	30	ns	336 (173)	0.414 (0.469)	20.9 (7.6)	29.4 (33.3)	147.2 (6.6)	148.7 (4.6)
WLST181	27	ns	455 (118)	0.160 (0.294)	29.1 (4.4)	11.4 (20.8)	138.6 (4.5)	139.7 (3.7)

[a] fs means femtosecond laser line scan; ns means nanosecond laser crater.

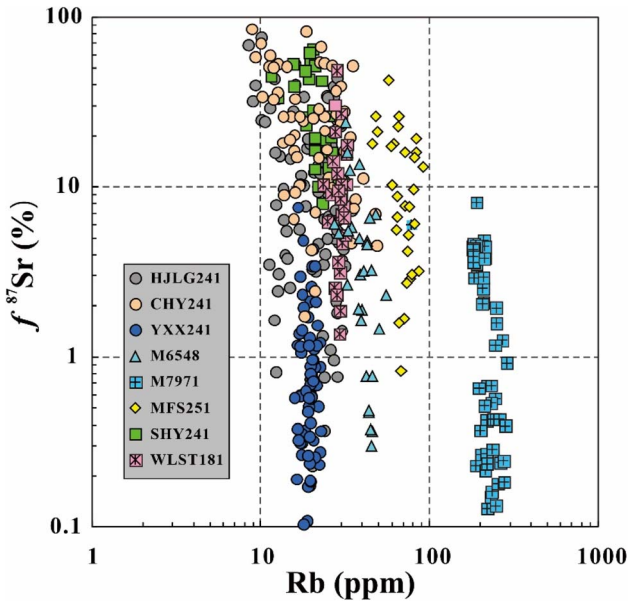

Fig. 7 The Rb content (ppm) and $f^{87}Sr$ in our beryl samples.

ratio of 0.22 ± 0.66 (Fig. 6a). The anchored diagram yielded an age of 1831 ± 15 Ma (n = 55; MSWD = 1.2). This sample shows low common Sr from 0.05% to 4.35%, with a median $f^{87}Sr$ value of 0.89 ± 1.76% (2σ, n = 55) (Table 4 and Fig. 7).

For the M6548 beryl, an unanchored diagram produced an age of 1778 ± 21 Ma (n = 30; MSWD = 1.3), with an initial $^{87}Sr/^{86}Sr$ ratio of 0.77 ± 0.16 (Fig. 5b). The anchored diagram yielded an age of 1784 ± 18 Ma (n = 30; MSWD = 1.3). This beryl shows variable common Sr contents from 0.08% to 24.13%, with a median $f^{87}Sr$ value of 4.73 ± 10.85% (2σ, n = 30) (Table 4 and Fig. 7).

The M7971 beryl produced an unanchored inverse isochron age of 240.2 ± 2.2 Ma (n = 38; MSWD = 6.2), with an initial $^{87}Sr/^{86}Sr$ ratio of 0.54 ± 0.34 (Fig. 6c). The anchored diagram gave an age of 239.6 ± 2.0 Ma (n = 38; MSWD = 4.6). These results agree well with the U–Pb age of those columbite group minerals, *ca.* 240 Ma (unpublished data), for pegmatite. This sample shows the lowest common Sr contents from 0 to 3.81% among the eight, with a median $f^{87}Sr$ value of 0.64 ± 2.28% (2σ, n = 38) (Table 4 and Fig. 7).

The MFS251 beryl gave an unanchored inverse isochron age of 151.3 ± 3.1 Ma (n = 30; MSWD = 0.2), with an initial $^{87}Sr/^{86}Sr$ ratio of 0.633 ± 0.096 (Fig. 5d). The anchored diagram yielded an age of 149.2 ± 2.3 Ma (n = 30; MSWD = 0.2). These results agree well with the zircon U–Pb age of *ca.* 145 Ma for Be-bearing pegmatite.[38] This sample also shows variable common Sr contents from 1.6% to 42.6%, with a median $f^{87}Sr$ value of 12.0 ± 19.2% (2σ, n = 30) (Table 4 and Fig. 7).

For the SHY241 beryl, the unanchored diagram yielded an age of 147.2 ± 6.6 Ma (n = 30; MSWD = 0.33), with an initial $^{87}Sr/^{86}Sr$ ratio of 0.733 ± 0.059 (Fig. 5e). The anchored diagram gave an age of 148.7 ± 4.6 Ma (n = 30; MSWD = 0.3). These results agree well with the monazite U–Pb age of *ca.* 145 Ma for granite.[39] This beryl has variable common Sr contents from 8.0% to 64.7%, with a median $f^{87}Sr$ value of 29.4 ± 33.3% (2σ, n = 30) (Table 4).

The WLST181 beryl produced an unanchored inverse isochron age of 138.6 ± 4.5 Ma (n = 30; MSWD = 0.3), with an initial $^{87}Sr/^{86}Sr$ ratio of 0.750 ± 0.077 (Fig. 5f). The anchored diagram yielded an age of 139.7 ± 3.7 Ma (n = 28; MSWD = 0.32). These results agree well with the cassiterite U–Pb age of *ca.* 136 Ma for Be-bearing pegmatite.[40] This beryl shows variable common Sr contents from 0 to 48.7%, with a median $f^{87}Sr$ value of 11.4 ± 20.8% (2σ, n = 28) (Table 4 and Fig. 7).

3.4 Comparative Rb–Sr geochronology of mica and beryl

Mica typically exhibits high Rb/Sr and is therefore well suited for Rb–Sr dating. With the advent of LA-ICP-MS/MS techniques, *in situ* Rb–Sr dating of biotite, muscovite, and phlogopite has become routine in many laboratories.[6–20] By contrast, beryl Rb–Sr geochronology has received comparatively limited attention, largely because beryl can contain only modest Rb (typically several tens of ppm).

As shown in Fig. 8, the Rb contents and $^{87}Rb/^{86}Sr$ ratios of the beryl samples are presented and compared with those of biotite, muscovite, and phlogopite previously reported by Huang *et al.*[16] (Fig. 8a). Our beryl suite displays Rb

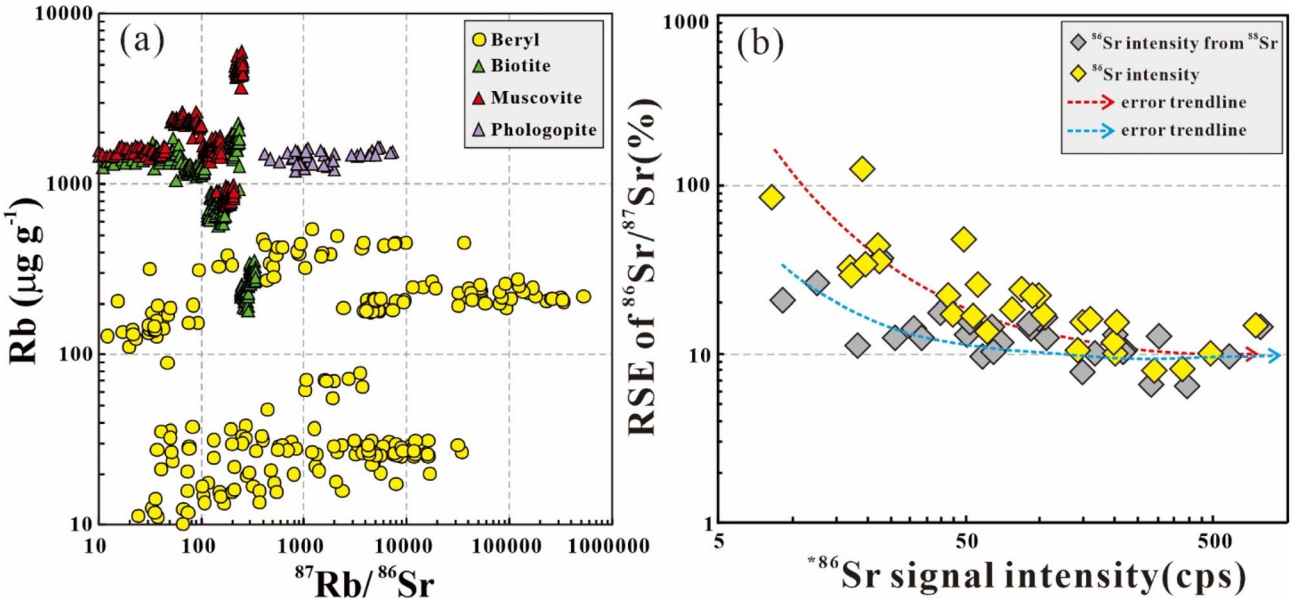

Fig. 8 The $^{87}Rb/^{87}Sr$ and Rb content between phlogopite, muscovite, biotite and beryl for comparison (a), indicating low Rb content and significant range of $^{87}Rb/^{87}Sr$ of beryl. The phlogopite, muscovite and biotite data are from Huang *et al.*[16] For beryl, the relative standard error (RSE) of $^{86}Sr/^{87}Sr$ relationship with ^{86}Sr signal intensity using direct ^{86}Sr measurement and calculated ^{86}Sr from ^{88}Sr signal intensity (b), indicating less RSE of $^{86}Sr/^{87}Sr$ ratio because of high abundance of ^{88}Sr compared with that of ^{86}Sr.

concentrations spanning ~2 orders of magnitude, whereas $^{87}Rb/^{86}Sr$ extends across ~5 orders of magnitude (~10 to 10^6) and thus yields almost wholly radiogenic ^{87}Sr. In combination, moderate Rb with extremely low Sr renders beryl highly amenable to Rb–Sr dating and, in favorable cases, permits robust single-mineral geochronology.

Because beryl typically contains a very low abundance of Sr, Sr-isotope precision is sensitive to ion signal intensity. Consistent with this, for beryl the relative standard error (RSE) of $^{86}Sr/^{87}Sr$ correlates with ^{86}Sr signal intensity (Fig. 7b). Calculating ^{86}Sr from the ^{88}Sr signal (given the much higher abundance of ^{88}Sr) yields smaller RSEs than direct ^{86}Sr measurement ($^{86}Sr/^{88}Sr = 0.1194$). Accordingly, ^{88}Sr-derived ^{86}Sr intensities were preferred in our analytical sessions.

To treat variable common Sr, data are presented as inverse-isochron arrays. This method allows explicit evaluation of common-Sr contributions and provides a test of geologic coherence *via* the linearity of the regression. All examined beryl samples define well-behaved (anchored or unanchored) inverse isochrons (Fig. 4–6), indicating closed-system behavior of Rb–Sr.

Beryl is stable over a broad range of temperatures (300–800 °C), fluid and rock compositions, and fO_2 conditions.[41] Nevertheless, late hydrothermal alteration can modify Rb–Sr systematics—typically *via* Rb or Sr mobility—yielding spuriously young ages; such effects are readily recognized petrographically. To distinguish crystallization ages from potential thermal-resetting, we calculated the Sr closure temperature in beryl following Zhao and Zheng,[41] assuming a nominal grain size of 10 mm and cooling rates of 10–200 °C Ma^{-1} (Fig. 9). The resulting closure temperatures of 650–800 °C are comparable to those of biotite and muscovite (700–800 °C for 1 mm grains). We therefore infer that unaltered beryl generally records the time of crystallization rather than a later isotopic closure. Consequently, where other dateable rare-metal phases are absent, pristine beryl constitutes a robust Rb–Sr chronometer for Be-mineralization systems.

3.5 Potential reference materials and implications for beryl Rb–Sr geochronology

Matrix effects between natural minerals and silicate-glass standards as reported in previous studies (*e.g.*, NIST SRM series) are well documented for elemental and isotopic ratios including Rb/Sr, Lu/Hf, and Re/Os.[15–19,21–23,42–44] Consequently, matrix-matched reference materials are required for accurate calibration.[10–13,18,19] A large (~1 cm^3) gem-quality aquamarine from the Erongo massif in Namibia, characterized by 40 ppm Rb, undetectable ^{86}Sr, and an age of 132 Ma, has been suggested as a promising candidate. However, to date no further comprehensive characterization has been published.[24]

In general, an ideal reference material for *in situ* Rb–Sr work should: (1) produce concordant (isochronous) results across distributed aliquots at the analytical scale of interest, without requiring perfect homogeneity; (2) possess a precise and accurate Rb–Sr age determined by matrix-independent methods (*e.g.*, ID-MS); (3) be readily obtainable in sufficient quantity; and (4) for beryl specifically, contain sufficient Rb and very low Sr so as to generate abundant radiogenic ^{87}Sr and high $^{87}Rb/^{86}Sr$, enabling precise ages by LA-ICP-MS/MS.[24,29,43]

Our results indicate that HJLG241 beryl of *ca.* 1800 Ma meets these criteria to a considerable extent: it has a mean Rb content of 26.82 ppm, abundant radiogenic ^{87}Sr, and spans wide ranges of $^{87}Rb/^{86}Sr$ and $^{87}Sr/^{86}Sr$. Similarly, CHY241 beryl, with an age of 1830 Ma, contains ~30 ppm Rb and exhibits a comparatively narrower spread in $^{87}Rb/^{86}Sr$ and $^{87}Sr/^{86}Sr$. Calibration of other

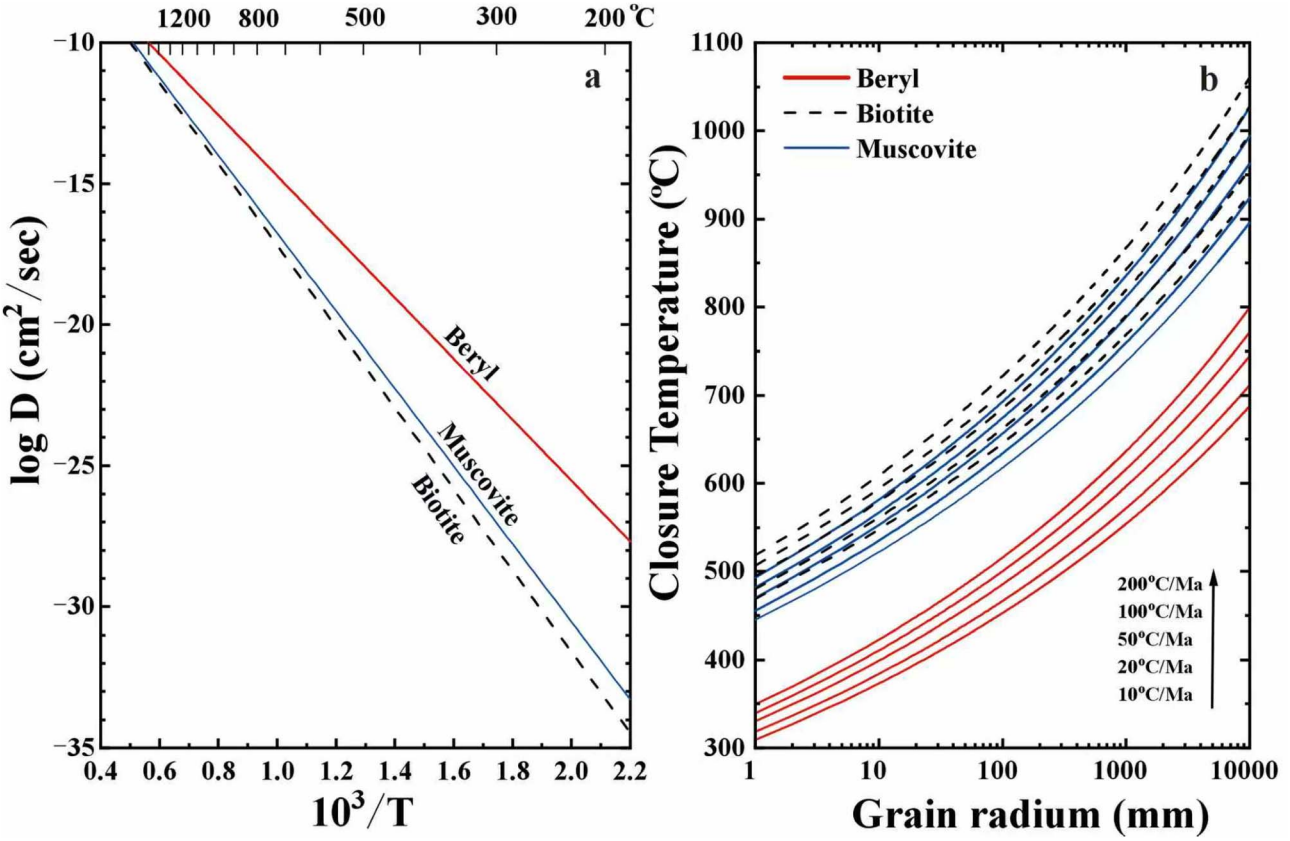

Fig. 9 Sr diffusion experiment simulation (a) and calculation of Sr closure temperatures in beryl, muscovite and biotite (b) based on the method of Zhao and Zheng.[41]

beryl samples against HJLG241 further supports its suitability as a primary matrix-matched reference material. In addition, M7971 contains ~300 ppm Rb and negligible common Sr. Although this composition is advantageous, further ID-TIMS characterization is required to constrain its initial $^{87}Sr/^{86}Sr$ and establish accurate Rb–Sr ages.

Given the diversity of gem-quality beryl varieties (aquamarine, emerald, heliodor, goshenite, morganite, and red beryl), previous studies have emphasized mineralogical attributes[3] and trace element chemistry.[4,25] The present study underscores the broader potential of beryl Rb–Sr geochronology,[24] with implications spanning Be-mineralization chronologies, tectono-magmatic reconstructions, and gemstone provenance. We anticipate that adoption of matrix-matched beryl reference materials such as HJLG241 (and, pending further validation, CHY241 and M7971) will facilitate routine, high-precision microbeam Rb–Sr dating of beryl in both geological and gemological contexts.[4,25]

4. Conclusions

Beryl, a widespread Be-bearing mineral in granitic pegmatites and mica schists, typically contains tens to hundreds of ppm Rb and exhibits high Rb/Sr ratios, leading to strongly radiogenic Sr. In this study, eight beryl samples spanning *ca.* 1.8–0.14 Ga were investigated to evaluate the feasibility of *in situ* Rb–Sr geochronology by LA-ICP-MS/MS. Age evaluation employed inverse-isochron regression to accommodate variable common Sr. The results demonstrate that *in situ* Rb–Sr dating of beryl by LA-ICP-MS/MS is practicable and yields precise, accurate ages that are concordant with solution Rb–Sr determinations and with U–Pb ages of coexisting accessory minerals. Estimates of the Sr closure temperature in beryl further support the interpretation that, in unaltered grains, Rb–Sr ages record crystallization rather than late isotopic resetting.

To enable routine application, we present an Iolite-based workflow comprising a DRS and the visual Rb–Sr Age plugin, which together permit end-to-end processing of laser-ablation Rb–Sr datasets. On the basis of ID-MS isochrons, two gem-quality beryl samples (HJLG241 and CHY241) are proposed as candidate primary reference materials for microbeam Rb–Sr geochronology, with ages of 1798 ± 13 Ma (2s, $n = 5$) and 1835 ± 8 Ma (2s, $n = 5$), respectively. More broadly, Rb–Sr geochronology of beryl, including varieties such as aquamarine, emerald, heliodor, goshenite, morganite, and red beryl, provides an independent chronometer capable of delivering robust age constraints, with significant implications for geochemical investigations and gemstone provenance studies.

Author contributions

Formal analysis: MP Zhang; conceptualization: YY Yang; methodology: C Huang and ST Wu; writing – draft: MP Zhang

and YH Yang; review: ZY Chu, ZF Zhao, H Wang, L Xu, JH Yang, and FY Wu; funding acquisition: YH Yang, LW Xie and ZY Chu.

Conflicts of interest

There are no conflicts to declare.

Data availability

The data that support the findings of this study are available in the supplementary information (SI) of this article. Supplementary information: Table S1: individual instrumental parameters for trace element and *in situ* Rb–Sr dating. Table S2: U-Pb age of HJLG241 monazite determined using LA-SF-ICP-MS including the analytical method and individual U–Pb data from the same place as HJLG241 beryl. Table S3: *in situ* Rb-Sr data obtained in analytical sessions using femtosecond or nanosecond lasers with TQ ICP-MS/MS. See DOI: https://doi.org/10.1039/d5ja00334b.

Crystals and fragments of beryl are available upon request for laboratories worldwide by contacting Prof. Y.H. Yang (e-mail: yangyueheng@mail.iggcas.ac.cn).

Acknowledgements

This work was financially supported by the Deep Earth Probe and Mineral Resources Exploration-National Science and Technology Major Project (2025ZD1005300) and Natural Science Foundation of China (42430105, 42522302 and 42473036). Cui TQ, Niu JL and Wang YJ are thankful for their mass spectrometric measurements. Thomas Zack is appreciated for thoughtful comments on our work during Goldschmidt2025 in Prague. We are also grateful to two reviewers for insightful comments that significantly improved this manuscript. Some chips of HJLG241 and CHY241 beryl samples can be obtained from Yueheng Yang (yangyueheng@mail.iggcas.ac.cn).

References

1 C. Klein and C. S. Hurlbut, *Manual of Mineralogy (After James D. Dana)*, John Wiley & Sons, New York, 21st edn, 1993, p. 472.
2 W. D. Nesse, *Introduction to Mineralogy*, Oxford University Press, Oxford, 2000, p. 301.
3 B. L. Sherriff and H. D. Grundy, *Can. Mineral.*, 1991, **29**, 271–285.
4 J. Y. Dong, F. Huang and D. H. Wang, *Acta Petrol. Sin.*, 2023, **39**, 2153–2166.
5 X. X. Ling, Q. L. Li, L. J. Feng, D. Zhang, Y. Liu, G. Q. Tang, J. Li, S. T. Wu, L. L. Huang, T. J. Li, Y. Liu, R. Werner and X. H. Li, *Crystals*, 2021, **11**, 1322.
6 T. Zack and K. J. Hogmalm, *Chem. Geol.*, 2016, **437**, 120–133.
7 K. J. Hogmalm, T. Zack, A. K. O. Karlsson, A. S. L. Sjöqvist and D. Garbe-Schönberg, *J. Anal. At. Spectrom.*, 2017, **32**, 305–313.
8 L. Gorojovsky and O. Alard, *J. Anal. At. Spectrom.*, 2020, **35**, 2322–2336.
9 D. Bevan, C. D. Coath, J. Lewis, J. Schwieters, N. Lloyd, G. Craig, H. Wehrs and T. Elliott, *J. Anal. At. Spectrom.*, 2021, **36**, 917–931.
10 A. Redaa, J. Farkas, S. Gilbert, A. S. Collins, B. Wade, S. Lohr, T. Zack and D. Garbe-Schonberg, *J. Anal. At. Spectrom.*, 2021, **36**, 322–344.
11 A. Redaa, J. Farkas, S. Gilbert, A. S. Collins, S. Lohr, D. Vasegh, M. Forster, M. Blades, T. Zack, A. Giulliani, R. Maas, A. Balderman, M. Dietzel and D. Garbe-Schonberg, *Geostand. Geoanal. Res.*, 2023, **47**, 23–48.
12 Y. Jegal, C. Zimmermann, L. Reisberg, D. Yeghicheyan, C. Cloquet, C. Peiffert, M. Gerardin, E. Deloule and J. Mercadier, *Geostand. Geoanal. Res.*, 2022, **46**, 645–671.
13 D. Rösel and T. Zack, *Geostand. Geoanal. Res.*, 2022, **46**, 143–168.
14 C. Y. Wang, O. Alard, Y. J. Lai, S. F. Foley, Y. S. Liu, J. Munnikhuis and Y. Wang, *Chem. Geol.*, 2022, **610**, 121073.
15 A. M. Cruz-Uribe, G. Craig, J. M. Garber, B. Paul, C. Arkula and C. Bouman, *Geostand. Geoanal. Res.*, 2023, **47**, 795–809.
16 S. Q. Huang, Z. S. Chang, K. R. Liu and D. Garbe-Schonberg, *Geostand. Geoanal. Res.*, 2023, **47**, 725–747.
17 C. Huang, H. Wang, W. B. Shi, J. F. Sun, F. Y. Hu, L. Xu, Y. H. Yang, S. T. Wu, L. W. Xie and J. H. Yang, *Sci. China Earth Sci.*, 2023, **66**, 2603–2621.
18 C. Huang, H. Wang, L. W. Xie, L. Xu, S. T. Wu, Y. H. Yang and J. H. Yang, *Spectrochim. Acta, Part B*, 2025, **224**, 107–117.
19 T. Zack and S. E. Gilbert, *Methods Appl. Geochronol.*, 2024, **7**, 211–241.
20 S. E. Gilbert, S. Glorie and T. Zack, *Methods Appl. Geochronol.*, 2024, **8**, 243–295.
21 S. T. Wu, H. Wang, Y. H. Yang, J. L. Niu, Z. W. Lan, L. L. Zhang, C. Huang, L. W. Xie, L. Xu, J. H. Yang and F. Y. Wu, *J. Anal. At. Spectrom.*, 2023, **38**, 1285–1300.
22 S. T. Wu, J. L. Niu, Y. H. Yang, H. Wang, J. H. Yang and F. Y. Wu, *J. Anal. At. Spectrom.*, 2024, **39**, 2703–2715.
23 S. T. Wu, Y. H. Yang, H. Wang, N. W. Roberts, J. L. Niu, Y. J. Wang, J. H. Yang and F. Y. Wu, *Chem. Geol.*, 2024, **670**, 122383.
24 T. Zack and K. Link, in *Goldschmidt Conference Abstracts*, 2019, vol. 1.
25 N. Daneshvar, H. Azizi, Y. Asahara, M. Tsuboi, M. Minami and Y. O. Mohammad, *Minerals*, 2021, **11**, 717.
26 S. T. Wu, G. J. Worner, K. P. Jochum, B. Stoll, K. Simon and A. Kronz, *Geostand. Geoanal. Res.*, 2019, **43**, 567–584.
27 Y. H. Yang, H. F. Zhang, Z. Y. Chu, L. W. Xie and F. Y. Wu, *Int. J. Mass Spectrom.*, 2010, **290**, 120–126.
28 Y. H. Yang, F. Y. Wu, Z. C. Liu, Z. Y. Chu, L. W. Xie and J. H. Yang, *J. Anal. At. Spectrom.*, 2012, **27**, 516–522.
29 Z. Y. Chu, T. Q. Cui, C. M. Thomas, Y. L. Li, C. F. Li, L. Xu, Y. H. Yang and P. Peng, *Geostand. Geoanal. Res.*, 2025, **49**, 1284–1301.
30 O. Nebel, K. Mezger, E. E. Scherer and C. Munker, *Int. J. Mass Spectrom.*, 2005, **246**, 10–18.
31 Z. Y. Chu, F. K. Chen, Y. H. Yang and J. H. Guo, *J. Anal. At. Spectrom.*, 2009, **24**, 1534–1544.

32 Z. C. Hu, S. H. Gao, Y. S. Liu, S. H. Hu, H. H. Chen and H. L. Yuan, *J. Anal. At. Spectrom.*, 2008, **23**, 1093–1101.
33 C. Paton, J. Hellstrom, B. Paul, J. Woodhead and J. Hergt, *J. Anal. At. Spectrom.*, 2011, **26**, 2508–2512.
34 P. Vermeesch, *Geosci. Front.*, 2018, **9**, 1479–1493.
35 Y. Li and P. Vermeesch, *Geochronology*, 2021, **3**, 415–420.
36 S. T. Wu and Y. H. Yang, in *Goldschmidt Conference Abstracts*, 2025, vol. 1.
37 M. S. A. Horstwood, J. Košler, G. Gehrels, S. E. Jackson, N. M. McLean, C. Paton, N. J. Pearson, K. Sircombe, P. Sylvester, P. Vermeesch, J. F. Bowring, D. J. Condon and B. Schoene, *Geostand. Geoanal. Res.*, 2016, 311–322.
38 P. F. Jiang, P. Li, J. K. Li, S. M. Li, X. Liu, S. B. Liu, C. H. Wang and D. F. Ji, *Miner. Depos.*, 2021, **40**, 723–739.
39 Z. P. Duan, S. Y. Jiang, H. M. Su, X. Y. Zhu, T. Zou and X. Y. Cheng, *Lithos*, 2021, **400–401**, 106415.
40 R. L. Liu, G. Wu, T. G. Li, G. Z. Chen, L. W. Wu, P. C. Zhang, T. Zhang, B. Jiang and W. Y. Liu, *Earth Sci. Front.*, 2018, **25**, 183–201.
41 Z. F. Zhao and Y. F. Zheng, *Am. Mineral.*, 2007, **92**, 289–308.
42 J. D. Woodhead and J. M. Hergt, *Geostand. Geoanal. Res.*, 2001, **25**, 261–266.
43 S. Glorie, S. E. Gilbert, M. Hand and J. C. Lloyd, *Geochronology*, 2024, **6**, 21–36.
44 P. Vermeesch, *Geochronology*, 2024, **6**, 397–407.